Investigation of the primary crystallization of Ni–17 at.% P alloy by ASAXS

D. Tatchev,[a]* G. Goerigk,[b,c] E. Valova,[a] J. Dille,[d] R. Kranold,[e] S. Armyanov[a] and J.-L. Delplancke[d]

[a]Institute of Physical Chemistry, Bulgarian Academy of Sciences, Sofia 1113, Bulgaria, [b]Institut für Festkörperforschung, Forschungszentrum Jülich, D-52425 Jülich, Germany, [c]DESY-HASYLAB, D-22603 Hamburg, Germany, [d]Université Libre de Bruxelles, Science des Matériaux et Electrochimie, B1050 Bruxelles, Belgium, and [e]Institut für Physik, Universität Rostock, Universitätsplatz 3, D-18051 Rostock, Germany. Correspondence e-mail: dtachev@ipc.bas.bg

Primary crystallization of Ni(P) particles in hypoeutectic Ni–P amorphous alloy obtained by electroless deposition has been investigated with ASAXS. The particle size distribution, the size dependence of the particle composition and the amorphous matrix composition were found simultaneously. The size distribution consists of a peak at particle radius of ~1 nm and a tail spanning from ~2 to 15 nm. The composition of the particles of the peak changes from ~14 to ~2 at.% P as their radius grows from 0.7 to about 3 nm. The particles in the tail of the size distribution (2–15 nm) have nearly constant P content in the range of 0–2 at.%. The matrix composition tends to the eutectic one at the end of the primary crystallization process.

1. Introduction

The so-called classical nucleation theory (see *e.g.* Christian, 1975; Kashchiev, 2000; Markov, 2002) is usually employed in the theoretical interpretation of nucleation–growth experiments. It is based on Gibbs' classical thermodynamic description of heterogeneous systems (Gibbs, 1928). However, in a number of cases, in particular for multicomponent systems, this theory is unable to give a satisfactory explanation of the experimental data. Gibbs' theory is restricted to thermodynamic equilibrium states, *i.e.* it is not suitable for the description of the properties of sub- and supercritical clusters and their development in the course of a phase-transformation process. Gibbs' nucleation theory is based on the condition that the critical nuclei have essentially the same state parameters as the corresponding newly evolving macroscopic phase. Recently, a generalization of Gibbs' classical approach has been developed which overcomes the aforementioned problems (Schmelzer *et al.*, 2000, 2004*a,b*). According to this new approach, both the structure and composition of real critical clusters may differ significantly from those of the corresponding macrophases. It turns out that, in general, the composition of the clusters should depend on their size and time of growth.

There are, however, few experimental methods allowing one to determine directly the size dependence of the cluster composition. In this paper we show that the size dependence of the cluster composition can be determined simultaneously with the particle size distribution by means of anomalous small-angle X-ray scattering (ASAXS) (Stuhrmann, 1985; Goerigk *et al.*, 2003). The investigated process is the primary crystallization of the amorphous electrolessly deposited Ni–17 at.% P alloy. This hypoeutectic alloy undergoes primary crystallization (Hornbogen, 1983) at elevated temperature (Bakonyi *et al.*, 1993; Hur *et al.*, 1990; Pittermann & Ripper, 1985, 1986; Wachtel *et al.*, 1991). Several authors assume that the precipitating Ni particles contain a certain amount of phosphorus during the transformation (Bakonyi *et al.*, 1993; Dietz & Schneider, 1990). Experimental research evidence for this assumption was given by Dietz & Schneider (1990) for electrodeposited Ni–P alloy. It is thus clear that for this binary system the simultaneous determination of particle composition and size distribution functions is important.

2. Theory

The determination of the size distribution of particles in a matrix from SAS data faces a mathematical inverse problem that can be generally expressed as (Feigin & Svergun, 1987; Glatter & Kratky, 1982)

$$I(s) = \int\limits_0^\infty X(R)A(s, R)\, dR, \qquad (1)$$

where $I(s)$ is the scattered intensity, $A(s, R)$ is the kernel of the integral equation, $X(R)$ is the sought function and $s = |\mathbf{s}| = (4\pi/\lambda)\sin(\theta)$ is the magnitude of the scattering vector; 2θ is the scattering angle, λ is the X-ray wavelength and R is the particle radius. Equation (1) formulates an ill-posed inverse problem, because from a finite number n of measured scattering intensity values $I(s_l)$, $l \in [1, n]$, the unknown distribution function $X(R_p)$, $p \in [1, m]$, in m points is sought. There

are several methods developed for its solution. The most common are integral transform techniques (Fedorova & Schmidt, 1978; Schmidt, 1981; Walter *et al.*, 1985), the inverse transformation method (Glatter, 1980) and the maximum entropy method (Potton *et al.*, 1983, 1988*a*,1988*b*; Tatchev & Kranold, 2004).

When looking for size-dependent particle composition and/or density, it is better to define the functions $X(R)$ and $A(s, R)$ as

$$X(R) = (\Delta\rho)^2(R)\, dw(R)/dR \qquad (2)$$

and

$$A(s, R) = v(R)\Phi^2(s, R). \qquad (3)$$

Here $\Delta\rho$ is the electron density difference between the particles and the matrix, $v(R)$ is the volume of a particle with radius R and dw/dR is the differential volume-fraction radius distribution function. The function $\Phi(s, R)$ is the normalized scattering amplitude of a single particle. It is considered to be known.

Using any of the aforementioned methods, one can find a distribution function $X_k(R)$ from several scattering curves measured at different X-ray energies near an absorption edge of an element contained in the sample (in the present case Ni). If the scattering contrast is a single-valued function of the particle radius, then the ratio $\Gamma_{ij}(R) = X_i(R)/X_j(R)$ between any two $X_k(R)$ will be a function of the particle composition and density only. Thus, measuring the scattering curves at a total of q values of the X-ray energy, E_i, one can form a system of $q - 1$ nonlinear equations of the type

$$\Gamma_{ij}(R) = \frac{[\Delta\rho(E_i, R)]^2}{[\Delta\rho(E_j, R)]^2}$$
$$= \frac{\left| f_p[E_i, C_p(R)]\eta_p[C_p(R)] - f_m(E_i, C_m)\eta_m(C_m) \right|^2}{\left| f_p[E_j, C_p(R)]\eta_p[C_p(R)] - f_m(E_j, C_m)\eta_m(C_m) \right|^2}, \qquad (4)$$

where

$$f_{p/m}(E_i, C_{p/m}) = f_A(E)C_{p/m} + (1 - C_{p/m})f_B(E) \qquad (5)$$

is the average atomic scattering amplitude for a binary alloy of constituents A and B, $C_{p/m}$ is the atomic part of the constituent A, f_A and f_B are the corresponding complex atomic scattering amplitudes,

$$f(E) = f_0 + f'(E) + if''(E), \qquad (6)$$

and the subscripts p and m denotes 'particles' and 'matrix', respectively.

The atomic density, $\eta_{p/m}(C_{p/m})$, depends on the composition trough the mass densities $d_{p/m}$ of the particles and the matrix,

$$\eta_{p/m}(C_{p/m}) = \frac{N_A d_{p/m}(C_{p/m})}{M_A C_{p/m} + (1 - C_{p/m})M_B}. \qquad (7)$$

$M_{A/B}$ are the atomic mass numbers of the two alloy constituents and N_A is Avogadro's number.

There are some interrelations between the variables in equation (4). The matrix composition, C_m, is connected with $dw(R)/dR$ and $C_p(R)$ through the mass conservation law. For binary alloy it reads

$$C_m = \frac{\overline{C} - \overline{\eta}^{-1}\int_0^\infty C_p(R)\eta_p(R)[dw(R)/dR]\, dR}{1 - \overline{\eta}^{-1}\int_0^\infty \eta_p(R)[dw(R)/dR]\, dR}, \qquad (8)$$

where $\overline{C}$ stands for the average A concentration of the alloy and the average atomic density of the alloy is given by

$$\overline{\eta} = \int\limits_0^\infty \eta_p(R)\frac{dw}{dR}(R)\, dR + (1 - w)\overline{\eta}_m \simeq \frac{d(\overline{C})N_A}{M_A\overline{C} + (1 - \overline{C})M_B}. \qquad (9)$$

Here $d(\overline{C})$ denotes the average matrix mass density. As, generally, SAS is applicable to particle size distribution determination only for diluted systems, the matrix composition and therefore the density will not change much. Therefore, $d(\overline{C})$ can be considered as constant.

The dependence of the particle density on the particle composition is generally unknown. Though the density of the bulk material with the same composition may be known, the density of the small particles may be different. Thus, we should consider both the composition and the density as independent unknown variables. Using at least three values of the X-ray energy near an absorption edge, the corresponding equations of the type (4) form a system for these two unknown variables for each value R_p of the particle radius. Solving this system would give both the composition and the density of the particles as a function of the particle radius. The scattering contrast could then be calculated and the particle size distribution could be obtained from any $X_k(R)$ in equation (2).

One should investigate the Jacobian of the system (4) to determine if it can be solved (at least numerically) for C_p and d_p. This has not yet been done to our knowledge. Instead, here we preferred to vary linearly the particle density as a function of composition. The reason is that the mass density difference between the pure Ni and the amorphous Ni–17 at.% P alloy is ~10.7%. Our ASAXS data definitely lack the accuracy to allow the determination of the composition and density of the particles with such precision.

The general procedure to determine simultaneously the size dependence of the particle composition and the size distribution is an iterative one. Starting with an arbitrary value of C_m one calculates $C_p(R)$ from equation (4), $dw(R)/dR$ from equation (2) and C_m from equation (8). The last C_m value is used to start a new calculation of $C_p(R)$, $dw(R)/dR$ and C_m. Calculation proceeds until the starting and final values of the matrix composition coincide. The $X_k(R)$ functions are determined only once from the scattering curves by the maximum entropy method (MEM). In the case of a high total volume fraction of the particles, the local monodisperse approximation with a hard-sphere interaction potential (Pedersen, 2002) could be applied. This leads to another iterative procedure that includes the already described procedure and the MEM fitting of the data. The adjusted parameter is the particle volume fraction.

3. Experimental

The amorphous Ni–17 at.% P alloy samples were obtained by electroless (autocatalytic) deposition from a citric acetic acidic bath (Armyanov *et al.*, 1982, 1986) on Al substrate. All samples were parts of one large specimen: Ni–P film, deposited on aluminium alloy substrate for a thin-film magnetic memory disk, rotated in the bath during plating to ensure uniform electroless deposition. The substrate was dissolved in a 20% solution of HCl acid. Smaller pieces were cut from the so-obtained foil. They were used for the annealing, ASAXS and transmission electron microscopy (TEM) experiments. The initial amorphous state of the samples was confirmed by X-ray diffraction. The chemical composition of the electrolessly deposited Ni–P film was determined by energy-dispersive X-ray spectroscopy. The accuracy of determination of the phosphorus content was ±0.5%.

The ASAXS experiments were performed at the JUSIFA beamline (Haubold *et al.*, 1989) at HASYLAB-DESY, Hamburg. The two-dimensional scattering patterns were measured in the energy range of the K-absorption edge of Ni at 8333 eV. The scattering patterns were normalized to the primary flux and corrected for background, dark current, detector sensitivity and sample transmission. The scattering curves obtained from the two-dimensional scattering patterns were calibrated into macroscopic scattering cross sections in units of cross section per unit volume $cm^2/cm^3 = cm^{-1}$. The basic data reduction and error determination were performed by standard procedures with instrument-dedicated software.

Two heat treatment procedures were applied. Four samples were annealed in a laboratory furnace at 515 K for time periods between 90 and 360 min. This sample set was

Figure 1
Ni–17 at.% P alloy annealed for 90 min at 515 K. Magnification 560000×. At least four particles with nearly spherical shape and radii of 1 to 5 nm are visible. The imaged area is 135 × 170 nm.

completed with one non-annealed sample. In the other case, one sample was annealed in the sample heater of the JUSIFA beamline at 523 K. To avoid extensive sample change during X-ray exposition, the sample was rapidly cooled to room temperature after every 90 min of annealing. The ASAXS measurements were performed at room temperature after each cooling. This procedure was applied until the sample had undergone a total of 360 min of annealing at 523 K. The heating and cooling between 523 K and room temperature took not more than 4 min.

The same X-ray energy values of 8033, 8298 and 8328 eV were used for the ASAXS measurements on both the pre-annealed and the stepwise-annealed samples.

After the ASAXS measurements, the sample structure was observed by TEM. The TEM foils were prepared using TENUPOL (Struers). The double-jet electrochemical thinning was performed with a solution of glacial acetic acid and perchloric acid (92.5% CH_2COOH and 7.5% $HClO_4$) at a temperature between 283 and 288 K and an applied voltage of 40 V.

TEM and SAD (selected area diffraction) studies were made using a Philips CM20 high-resolution transmission electron microscope at an accelerating voltage of 200 kV.

4. Results

4.1. TEM

The TEM images of the as-obtained (non-annealed) sample of the amorphous Ni–17 at.% P alloy are featureless. Thus it can be accepted that the as-obtained alloy is homogeneous down to the scale of about 1 nm.

Particles with sizes from approximately 1 to 12 nm appear after annealing at 515 K for periods from 90 to 360 min. Fig. 1 shows four such particles with different radii ranging from about 1 to 5 nm. Their shapes are close to spherical. With further annealing the particles grow larger. The largest particle ever observed in a total of 17 TEM images had a radius of about 15 nm. Twins and stacking faults appear frequently in crystalline particles with size above 3–4 nm (Fig. 2). The larger particles often display faceting. Occasionally, ribbed particles appear. In general, the particle shape is close to globular.

Despite the presence of crystalline particles, their volume fraction is insufficient to give spotted rings on the corresponding selected area diffraction pattern. Only the pattern of the sample annealed at 523 K for 360 min contains faint spotted rings superimposed on the amorphous halo.
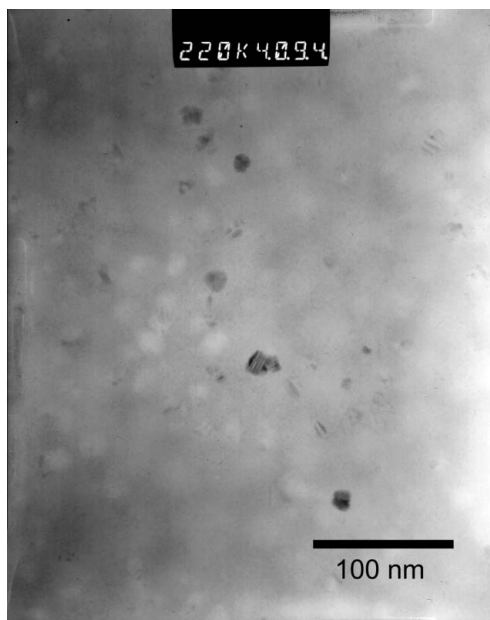
4.2. ASAXS

The scattering curves at an X-ray energy of 8033 eV of the four samples annealed at 515 K together with that of the as-obtained sample are shown in Fig. 3. The scattering curves change with the annealing time. Two areas can be distinguished. The curves change weakly for $s < 0.2$ nm^{-1} and more strongly at $s > 0.2$ nm^{-1}. Analogous behaviour is observed for
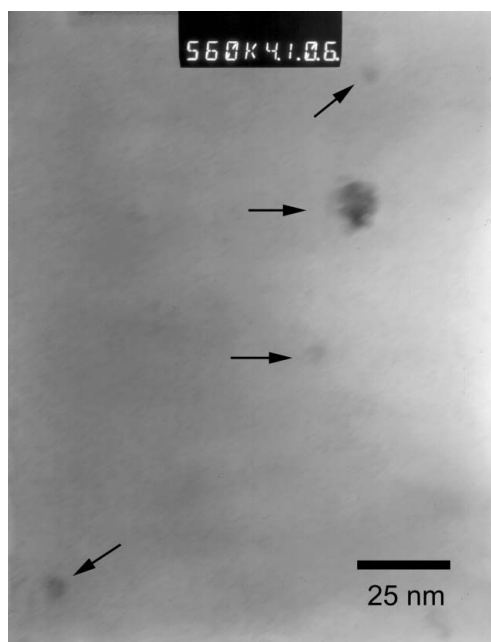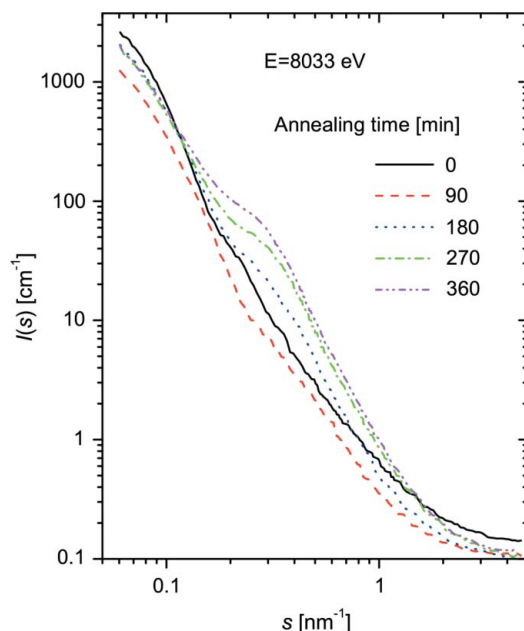
the sample annealed at 523 K (Fig. 4), but obviously a more advanced stage of the transformation is achieved.

Looking at the scattering behaviour at large s values, the Porod (1951) law is never observed. Rather, a power law, $I(s) \simeq s^{-\alpha}$, could fit the data. The values of the exponent α range from 2.4 to 3.8 and increase with the annealing time. In any case, the value of α depends on the smallest s value used for the fit. The attempts to determine and subtract the constant background using this power law usually resulted in negative values of scattering intensities in the range $s > 1 \te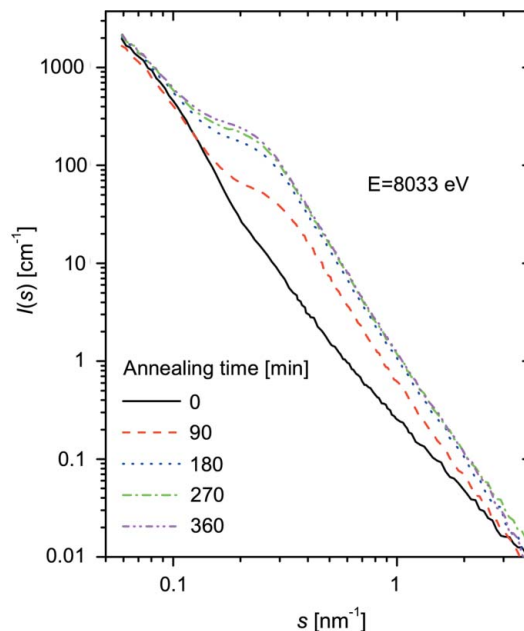xt{ nm}^{-1}$. Thus the scattering background was determined directly from the scattering curves. Since the curves reach a nearly constant scattering level for $s > 3$–4 nm^{-1}, as in Fig. 3, the scattering background was determined by averaging the last 8–10 points of the scattering curve. The curves in Fig. 4 have the background subtracted.

Fig. 5 gives a notion of the magnitude of the anomalous effect. The decrease in intensity is stronger in the region $s \geq 0.2 \text{ nm}^{-1}$, indicating that Ni-rich structures correspond to this scattering contribution. In comparison, the energy dependence of the scattering contributions in the range $s \leq 0.1 \text{ nm}^{-1}$

Figure 2
TEM micrograph of an Ni–17 at.% P sample annealed for 180 min at 515 K. Magnification 220000×. The imaged area is 340 × 440 nm.
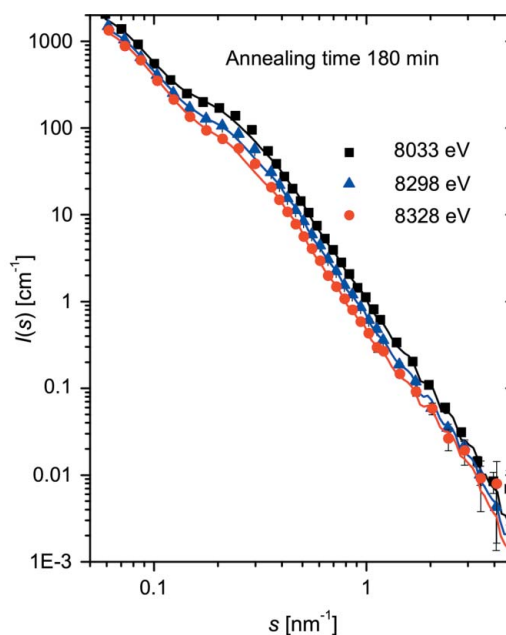

Figure 4
Scattering curves of the samples stepwise annealed at 523 K. The constant background is subtracted.

Figure 3
Scattering curves of the samples pre-annealed at 515 K.

Figure 5
MEM fits of the scattering curves of the sample annealed for 180 min at 523 K. Not all measuring points of the scattering curves are drawn.

show a behaviour which is governed by the squared average atomic scattering amplitude of the entire alloy $|f_{av}|^2 = |0.83f_{Ni} + 0.17f_P|^2$. When normalized to this quantity, the scattering curves from the three different energies nearly match, indicating that the scattering curves at smallest s values are probably dominated by the scattering of large surface structures. These surface structures change only slightly during the annealing under vacuum (Fig. 4), but markedly during the annealing in air (Fig. 3). For this reason, the scattering curves in Fig. 3 do not seem to follow the annealing time sequence. It should also be kept in mind that the different samples sometimes show individual behaviour. The scattering curves in Fig. 4 are obtained from the same volume element of the sample.

Typical maximum entropy fits of the scattering curves are likewise shown in Fig. 5. Two radii distributions were used to fit the data. The first spans from 0.5 to 15 nm and corresponds to the particle sizes observed by TEM. The second is a dummy one and lays in the interval 16–50 nm. Its contribution prevails in the scattering curve for $s < 0.15$ nm^{-1}, but implies a correction of the entire scattering curve. For both size distributions, the form factor $\Phi^2(s, R)$ of a homogeneous spherical particle (Guinier & Fournet, 1955) is used. Only the first size distribution is considered further, since it corresponds to the particles of interest.

An example of the contrast ratios obtained, $\Gamma_{ij}(R)$, is depicted in Fig. 6. The horizontal lines mark the level for particles of pure Ni ($d_p = 8.9$ g cm^{-3}). Values of $\Gamma_{ij}(R)$ above or equal to this level have physical meaning. Since there are some points below it, we applied a smoothing procedure. The running-average smoothing method was employed using eight or ten nearest points. The smoothed curves are also shown in Fig. 6. The particle composition was determined from the smoothed curves. Linearly varying particle density was used according to $d_p(C_p) = (8.9 - 3.0C_p)$ g cm^{-3}. The matrix density was kept equal to the experimentally determined density of the as-obtained sample, namely 8.0 g cm^{-3}. The iterative procedure for determination of the particle composition converges after not more than four iterations. The calculation for the samples annealed at 523 K was repeated with an external iterative loop to account for interparticle interference effects. This loop also converges after about four iterations.

Figs. 7 and 8 represent the differential volume-fraction size distributions and the size dependence of the composition of the particles for the samples annealed at 515 and 523 K, correspondingly. The size distributions for both annealing temperatures show qualitatively the same features: a peak at a radius of approximately 1 nm and a tail, or another broad peak, spanning from about 2 to 15 nm. The first peak at 1 nm is the highest in the size distributions for both temperatures. The volume fraction and number of both the smaller (0.5–2 nm) and larger (2–15 nm) particles increase with the annealing time. The size distributions in Figs. 7(a) and 8(a) follow the annealing time sequence, which means that the parasitic scattering is reliably separated.

The phosphorus content decreases monotonically with the increase of the particle size. The particles of smallest size may
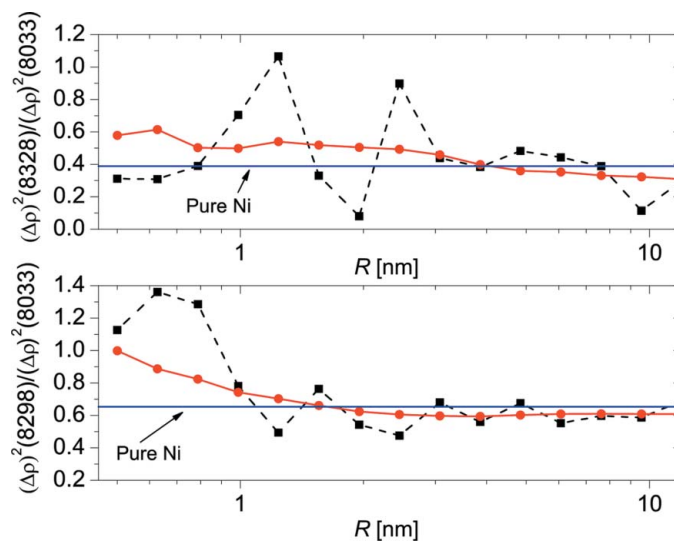
Figure 6
Contrast ratios for the sample annealed at 515 K for 360 min (squares). The numbers in the brackets in the ordinate label are the X-ray energies (eV). Circles are obtained by smoothing of the eight nearest neighbours.

contain up to 14 at.% P. The particles with radii greater than 2–3 nm contain less than 2 at.% P. The change of the composition–size curves with annealing time does not seem to be systematic, especially for the samples annealed at 523 K. For this reason, the four composition–size curves given in Figs. 7(b) and 8(b), respectively, were averaged and presented as a single curve without symbols, as a general description of the observed tendency.

The increase of the volume fraction, w, of the particles with annealing time is shown in Fig. 9. The maximum values of w calculated from the scattering curves are 6.1 and 10.1% for temperatures of 515 and 523 K, correspondingly. The maximum phosphorus contents of the matrix are 17.9 and 18.4 at.%, respectively. The volume-fraction curves were extrapolated to infinite annealing time by the Kolmogorov–Johnson–Mehl–Avrami (KJMA) method (see *e.g.* Christian, 1975). The volume fractions that would be reached after infinite annealing time are $(7 \pm 3)\%$ and $(9.0 \pm 0.7)\%$ for 515 and 523 K, respectively. The calculated average matrix compositions corresponding to these values of the volume fraction are (18.0 ± 0.7) and (18.4 ± 0.1) at.% P.

Fig. 9 shows also the volume fraction and the average matrix composition for the sample annealed at 523 K calculated considering interparticle interference effects. The interparticle interference does not seem to be significant in this case.
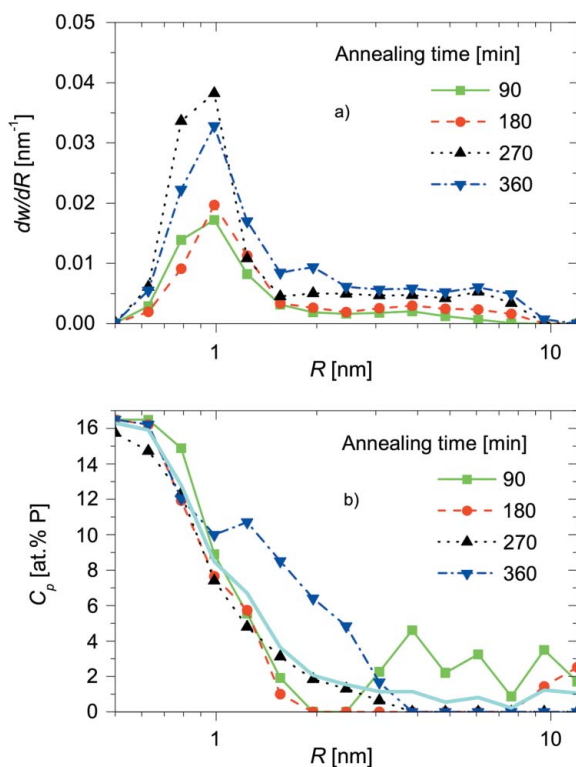
5. Discussion

Here we used only three values of the X-ray energy. However, a larger number of energies would be beneficial and desirable because a larger number of squared contrast ratios could be obtained. This is helpful for a more accurate determination of the composition from the system of equations (4). Moreover, the particle density could also be treated as a free parameter. Thus, using *ASAXS*, a potential opportunity exists for the
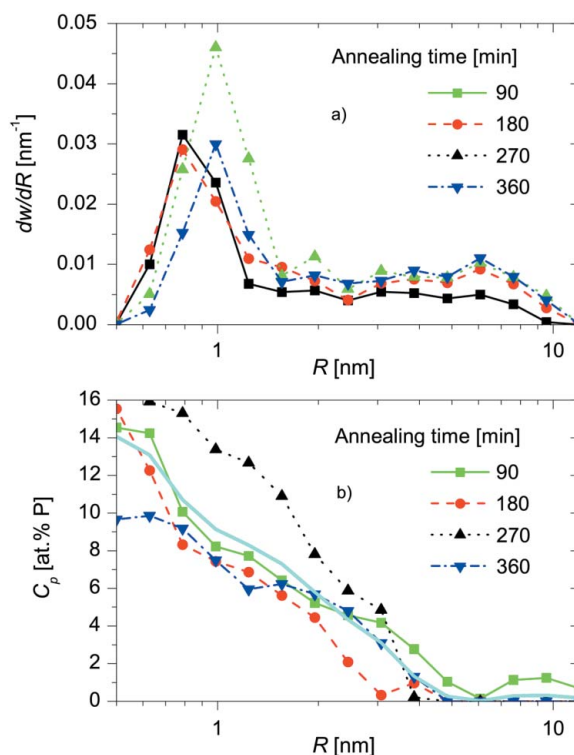
determination of particle density and composition as a function of the particle size together with the particle size distribution. It is easy to show that if the composition and the density of the particles are not single-valued functions of the particle size, then the size-averaged squared contrast is determined and used in equation (4), at least for the case of diluted systems.

The inspection of the TEM images (Figs. 1 and 2) shows that an appropriate scattering form factor, $\Phi^2(s, R)$, is that of spherical particles. This is the best choice, though the shape of the Ni(P) particles is globular rather than spherical. A greater problem is the additional scattering effect already appearing in the scattering curves of the as-obtained samples (Figs. 3 and 4). Obviously, this scattering comes from certain structures larger than the Ni(P) particles and most probably located on the sample surface. It should be mentioned that these large-scale structures have no magnetic contrast in SANS. Because the parasitic scattering effect changes slightly with annealing time, an additional dummy size distribution was used to 'fit' the lowest-s part of the scattering curves. This is advantageous since the dummy size distribution applies also some correction (Porod law) to the entire scattering curves.

The linear dependence of the particle density on particle composition was selected according to Bennett & Watson (1993) and Dietz & Schneider (1990). Anyway, the slopes of this dependence given in the mentioned sources are too high to comply with our experimental data. We used the maximum possible slope of $3.0C_p$. Thus, the density of (hypothetic)

Figure 8
Particle size distributions, (a), and size dependence of the particle composition, (b), for the samples annealed at 523 K. The line without symbols is an average for all annealing times.

Figure 7
Particle size distributions, (a), and size dependence of the particle composition, (b), for the samples annealed at 515 K. The line without symbols is an average for all annealing times.
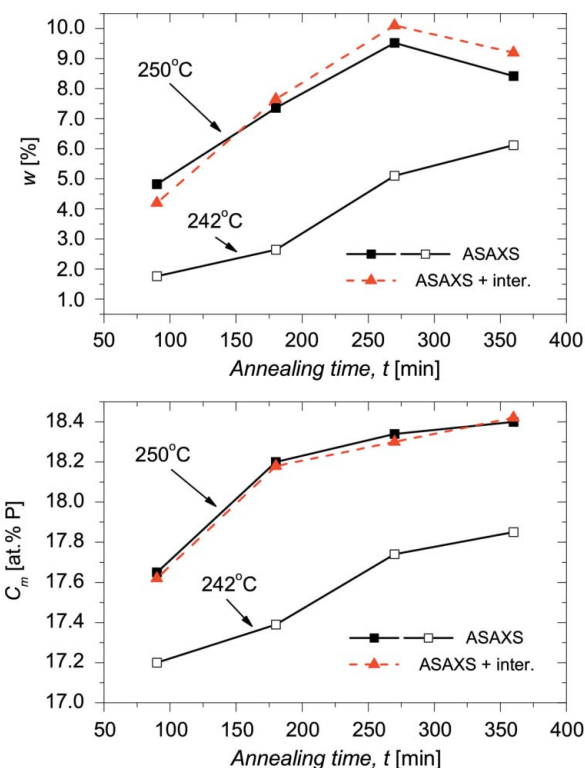
Figure 9
Increase of the volume fraction, w, and the average composition of the amorphous matrix, C_m, with annealing time. Squares: calculation without interparticle interference; triangles: calculation with interparticle interference.

particles with C_p = 17 at.% P is higher than the density of the amorphous matrix. This is expected, since the particles are crystalline. Actually, the density dependencies given by Bennett & Watson (1993) and Dietz & Schneider (1990) refer to bulk (foil) samples that may not be homogeneous. The actual particle density may be different from that of the bulk material, so that equality of our density–composition dependence to the previously measured one is not necessary.

The differential volume-fraction size distributions in Figs. 7(a) and 8(a) have essentially similar shape. The particle radii determined by TEM, 1–15 nm, coincide with those determined by ASAXS. Integration of the differential number density size distributions, corresponding to the distributions in Figs. 7(a) and 8(a), shows that the number of both the smaller (0.7–2.0 nm) and the larger (above 2 nm) particles increases with annealing time for both temperatures. The increase of the volume fraction of the larger particles is faster at the higher annealing temperature, 523 K, as expected. The size distributions in Fig. 7(a) represent earlier stages of transformation than the distributions in Fig. 8(a). The size distribution obtained for 90 min annealing at 523 K is very similar to those for 270 and 360 min at 515 K. The total volume fraction as a function of annealing time (Fig. 9) is s-shaped for the annealing temperature of 515 K, but increases with saturation for annealing at 523 K. All these findings indicate that the lower annealing temperature of 515 K allows the observation of earlier stages of the transformation, while the later stages were studied at 523 K.

The phosphorus content of the particles decreases monotonically from 10–14 at.% to 0–2 at.% if the particle radii increase from 0.7 to 2–3 nm [see the lines without symbols in Figs. 7(b) and 8(b)]. It seems that at lower temperature this decrease is steeper and particles with 2 nm radius already contain less than 2 at.% P. At the annealing temperature of 523 K, particles with radii greater than 4 nm have this composition. In any case, the data error is too large to make firm conclusions.

The matrix composition (Fig. 9) changes by not more than 1 at.% during the period of observation. The matrix compositions calculated for infinite annealing time at both annealing temperatures do not exceed the eutectic composition of 19 at.%. Allowing for the error of the composition determination, we can conclude that the process of primary crystallization in the investigated alloy will continue until the composition of the matrix reaches the eutectic composition. Though expected, such a result had not been experimentally proved before.

The results obtained show that neither the composition nor the density of the supercritical clusters are equal to the corresponding parameters of the newly evolving macroscopic phase, i.e. pure Ni. The composition and the density of the smallest particles are closer to the corresponding parameters of the matrix than to those of pure Ni, despite the fact that the equilibrium bulk phase is pure Ni (Massalski, 1986). This conclusion supports the new theoretical approach proposed by Schmelzer et al. (2000, 2004a,b).

6. Conclusions

It is possible from ASAXS experiments to determine simultaneously the differential volume-fraction size distribution and the composition size distribution of a diluted system of particles in a matrix by using the ratio between the contrasts obtained from scattering curves taken at different X-ray energy values. The mass conservation law must be used as an additional equation. The ratio between the contrasts is found from the ratio between two solutions of an integral equation with scattering data corresponding to different X-ray energies.

Annealing of amorphous Ni–17 at.% P alloy at 515 and 523 K results in precipitation of Ni-rich particles. Their differential volume-fraction size distribution consists of a peak at particle radius of 1 nm and a tail spanning from 2 to 15 nm. The phosphorus content of the particles of the peak decreases from ∼14 to ∼2 at.% as the radius grows from 0.7 to 2–3 nm. The particles of the tail have constant composition between 0 and 2 at.% phosphorus. These findings, based on our analysis of experimental data, comply with the new nucleation theory developed by Schmelzer et al. (2000, 2004a,b).

The volume fraction of the Ni(P) particles increases with increasing annealing time. The P content of the matrix increases by about 1 at.%. Extrapolation to infinite annealing time implies that at the end of the primary crystallization the matrix composition tends to the eutectic one. To our knowledge, this result is the first experimental proof of the theoretically expected product of the phase transformation in hypoeutectic Ni–P amorphous alloy.

References

Armyanov, S. A., Chakarova, G., Vangelova, T. & Pozharlieva, Ts. (1986). Bulgarian Patent No. 47282.

Armyanov, S. A., Vangelova, T. & Stoyanchev, R. (1982). *Surf. Technol.* **17**, 89–100.

Bakonyi, I., Burgstaller, A., Socher, W., Voitländer, J., Toth-Kadar, E., Lovas, A., Ebert, H., Wachtel, E., Willmann, N. & Libermann, H. H. (1993). *Phys. Rev. B*, **47**, 14961–14976.

Bennett, L. H. & Watson, R. E. (1993). *J. Alloys Compd.* **197**, 271–280.

Christian, J. W. (1975). *The Theory of Transformations in Metals and Alloys*, 2nd ed. Oxford University Press.

Dietz, G. & Schneider, H. D. (1990). *J. Phys. Condens. Matter*, **2**, 2171–2178.

Fedorova, I. S. & Schmidt, P. W. (1978). *J. Appl. Cryst.* **11**, 405–411.

Feigin, L. A. & Svergun, D. I. (1987). *Structure Analysis by Small-Angle X-ray and Neutron Scattering.* New York: Plenum Press.

Gibbs, J. W. (1928). *The Collected Works.* New York: Longmans and Green.

Glatter, O. (1980). *J. Appl. Cryst.* **13**, 7–11.

Glatter, O. & Kratky, O. (1982). *Small Angle X-ray Scattering.* London: Academic Press.

Goerigk, G., Haubold, H.-G., Lyon, O. & Simon, J.-P. (2003). *J. Appl. Cryst.* **36**, 425–429.

Guinier, A. & Fournet, G. (1955). *Small-Angle Scattering of X-rays.* New York: Wiley.

Haubold, H.-G., Gruenhagen. K., Wagener, M., Jungbluth, H., Heer, H., Pfeil, A., Rongen, H., Brandenburg, G., Moeller, R., Matzerath, J., Hiller, P. & Halling, H. (1989). *Rev. Sci. Instrum.* **60**, 1943–1946.

Hornbogen, E. (1983). *J. Mater. Sci.* **18,** 127–132.

Hur, K.-H., Jeong, J.-H. & Lee, D. N. (1990). *J. Mater. Sci.* **25**, 2573–2584.

Kashchiev, D. (2000). *Nucleation: Basic Theory with Applications.* Oxford: Butterworth-Heinemann.

Markov, I. (2002). *Crystal Growth for Beginners*, 2nd ed. Singapore: World Scientific.

Massalski, T. B. (1986). *Binary Alloy Phase Diagrams.* Ohio: ASM.

Pedersen, J. S. (2002). *Neutrons, X-rays and Light*, edited by P. Lindner & Th. Zemb, pp. 391–420. Amsterdam: Elsevier.

Pittermann, U. & Ripper, S. (1985). *Rapidly Quenched Metals*, edited by S. Steeb & H. Warlimond, p. 385. Amsterdam: Elsevier.

Pittermann, U. & Ripper, S. (1986). *Phys. Status Solidi A*, **93**, 131–142.

Porod, G. (1951). *Kolloid-Z.* **124**, 83–113.

Potton, J. A., Daniell, G. J., Eastop, A. D., Kitching, M., Melville, D., Poslad, S., Rainford, B. D. & Stanley, H. (1983). *J. Magn. Magn. Mater.* **39**, 95–98.

Potton, J. A., Daniell, G. J. & Rainford, B. D. (1988*a*). *J. Appl. Cryst.* **21**, 663–668.

Potton, J. A., Daniell, G. J. & Rainford, B. D. (1988*b*). *J. Appl. Cryst.* **21**, 891–897.

Schmelzer, J. W. P., Abyzov, A. S. & Möller, J. (2004*a*). *J. Chem. Phys.* **121**, 6900–6917.

Schmelzer, J. W. P., Gokhman, A. R. & Fokin, V. M. (2004*b*). *J. Colloid Interface Sci.* **272**, 109–133.

Schmelzer, J. W. P., Schmelzer, J Jr & Gutzow, I. S. (2000). *J. Chem. Phys.* **112**, 3820–3831.

Schmidt, P. W. (1981). *Diffraction Studies on Non-Crystalline Substances*, edited by I. Hargittai & W. J. Orville-Thomas, pp. 603–663. Budapest: Akadémiai Kiadó.

Stuhrmann, H.-B. (1985). *Adv. Polym. Sci.* **67**, 123–163.

Tatchev, D. & Kranold, R. (2004). *J. Appl. Cryst.* **37**, 32–39.

Wachtel, E., Bakonyi, I., Bahle, J., Willmann, N., Burgstaller, A., Socher, W., Voitländer, J., Lovas, A. & Libermann, H. H. (1991). *Mater. Sci. Eng. A*, **133**, 196–201.

Walter, G., Kranold, R., Gerber, Th., Baldrian, J. & Steinhart, M. (1985). *J. Appl. Cryst.* **18**, 205–213.